UC Berkeley
UC Berkeley Previously Published Works

Title
Using structural disorder to enhance the magnetism and spin-polarization in Fe x Si1???x thin films for spintronics

Authors
Karel, J
Zhang, YN
Bordel, C
et al.

Peer reviewed

Using structural disorder to enhance the magnetism and spin-polarization in Fe$_x$Si$_{1-x}$ thin films for spintronics

J Karel[1,2], Y N Zhang[3], C Bordel[2,4,5], K H Stone[2], T Y Chen[6], C A Jenkins[7], David J Smith[6], J Hu[3], R Q Wu[3], S M Heald[8], J B Kortright[2] and F Hellman[1,2,4]

[1] Department of Materials Science and Engineering, University of California, Berkeley, CA 94720, USA
[2] Materials Science Division, Lawrence Berkeley National Lab, Berkeley, CA 94720, USA
[3] Department of Physics and Astronomy, University of California, Irvine, CA 92697, USA
[4] Physics Department, University of California, Berkeley, CA 94720, USA
[5] GPM, UMR 6634 CNRS-Université de Rouen, 76801 St. Etienne du Rouvray, France
[6] Department of Physics, Arizona State University, Tempe, AZ 85287, USA
[7] Advanced Light Source, Lawrence Berkeley National Lab, Berkeley, CA 94720, USA
[8] Advanced Photon Source, Argonne National Laboratory, Argonne, IL 60439, USA
E-mail: julie.karel@cpfs.mpg.de

Abstract

Amorphous Fe$_x$Si$_{1-x}$ thin films exhibit a striking enhancement in magnetization compared to crystalline films with the same composition ($0.45 < x < 0.75$), and x-ray magnetic circular dichroism reveals an enhancement in both spin and orbital moments in the amorphous films. Density functional theory (DFT) calculations reproduce this enhanced magnetization and also show a relatively large spin-polarization at the Fermi energy, also seen experimentally in Andreev reflection. Theory and experiment show that the amorphous materials have a decreased number of nearest neighbors and reduced number density relative to the crystalline samples of the same composition; the associated decrease in Fe-Si neighbors reduces the hybridization of Fe orbitals, leading to the enhanced moment.

S Online supplementary data available from stacks.iop.org/MRX/1/026102/mmedia

Spintronic (spin-electronic) devices are a potential alternative to standard charge-based devices where the electron spin carries the information instead of the charge. Many proposed spintronic devices require a spin-injector, a material that can produce a highly spin-polarized current, and consequently significant work has gone into identifying these types of materials. $Ga_yMn_{1-y}As$, the canonical dilute magnetic semiconductor, has been touted as a promising material in this capacity. However, the Curie temperature remains low ($\sim$150 K), making the material unsuitable for room-temperature spintronic applications. By contrast, Fe_xSi_{1-x} alloys are potential candidates given their high Curie temperature and the tunability of their magnetic and electronic properties (including carrier concentration) with changes in the composition ($0.50 < x < 0.75$) of crystalline films [1–5]. This tunability comes in part because there exist three different bcc-like structures ($D0_3$, B2, A2), each with different degrees of chemical order. What has not been considered is the use of *structural* disorder to tune the magnetic and electronic properties, despite the fact that the mobility of the spin injector is not directly relevant and there are numerous examples of amorphous ferromagnets [6].

In this paper, we will show that amorphous (*a*-) Fe_xSi_{1-x} ($0.45 \leqslant x \leqslant 0.75$) is not only ferromagnetic but exhibits a significant *enhancement* in magnetic moment (both spin and orbital components) and spin polarization at the Fermi energy compared to crystalline counterparts. This enhanced magnetism is particularly surprising when considered in the context of magnetism in amorphous transition metals and their alloys, where the moments are strongly influenced by the local chemical environments. In many transition metal–metalloid (TM-M) alloys, the moment extrapolated to a pure amorphous transition metal is essentially the same as for the crystalline metal e.g. 1.7 μ_B/Co in a-Co_xP_{1-x} and 2.3 μ_B/Fe in a-Fe_xB_{1-x} as x approaches 1.0, and is reduced for lower x [7]. In addition, magnetic moments are often reduced from the crystalline counterpart by frustrated exchange interactions [7]. For example, vapor-quenched amorphous Fe was found to be ferromagnetic at low temperature but with a decreased average magnetic moment (1.5 μ_B/Fe) [8, 9] attributed to a distribution of interatomic distances leading to both positive (similar to α-Fe) and negative exchange interactions (similar to γ-Fe). Additionally, many amorphous Fe_yZ_{1-y} alloys (Z = Nb, Ta, Y, Zr, Lu) are ferromagnetic as y approaches 1, with moments ranging from 0.7–1.8 μ_B/Fe depending on y and Z, but all exhibit spin glass behavior with decreasing y ($y = 0.64$–0.80) due to frustrated mixed interactions [10–14].

By contrast, limited previous reports on amorphous Fe_xSi_{1-x}, show the onset of a magnetic moment occurs at $x = 0.4$, with a magnetization that increased with x [15–17] (e.g. 1.4 μ_B/Fe for $x = 0.62$), and no sign of frustration. However, the origin of the enhanced moment (versus the crystalline materials) was not explained, inhomogeneity was evidenced by the lack of square $M(H)$ curves, and structural analysis showed high local coordination, inconsistent with a ferromagnetic Fe alloy [17]. In this report, we investigate the structural, magnetic, and electronic properties of amorphous Fe_xSi_{1-x} and use density, DFT calculations and XAFS experiments to show that the enhanced magnetism is attributable to decreased coordination (below that of *either* bcc or fcc Fe) and a decrease in Si neighbors around each Fe atom, resulting in reduced *sd* hybridization.

The equilibrium phases in the investigated range of x are $D0_3$ ($x = 0.75$) and a large unit cell ε phase ($x = 0.5$) with exotic magnetic and transport properties, which will not be discussed [18]. Non-equilibrium bcc-like structures are possible with thin film growth: A2 (chemically disordered, random bcc solid solution), B2 (partially ordered, CsCl structure with Fe on the cube corner sites and Fe/Si randomly arranged on the body center sites) and finally $D0_3$

(chemically ordered, Fe on the cube corners and Fe and Si alternating in the body centers with excess Fe ($x > 0.75$) or excess Si ($x < 0.75$) randomly on the other's body center sites).

Fe_xSi_{1-x} thin films (1300–2200 Å) were grown by electron beam co-evaporation of Fe and Si. Amorphous films ($x = 0.45$–0.65) were grown at room temperature on amorphous SiN_x on Si substrates, and epitaxial Fe_xSi_{1-x} thin films ($x = 0.55$–0.75) were obtained by deposition on (001) MgO at 200 °C for $x > 0.65$. For epitaxial samples with $x \leqslant 0.65$, a Cr layer, deposited at 200 °C on (001) MgO prior to film growth, was required to obtain epitaxy[9]. Film number densities, n_{total}, and compositions were measured using Rutherford backscattering spectrometry (RBS). X-ray diffraction (XRD) and high-resolution transmission electron microscopy (HRTEM) were used to characterize the structure. Room temperature x-ray absorption fine structure (XAFS) was performed at the Fe K-edge at beamline 20-BM at the Advanced Photon Source. Magnetization (*M*) as a function of field (*H*) and temperature (*T*) was measured using a Quantum Design PPMS magnetometer. Room temperature x-ray absorption spectroscopy (XAS) and x-ray magnetic circular dichroism (XMCD) were performed in total electron yield at the Fe $L_{2,3}$-edge in a magnetic field of ±0.5 T at BL 6.3.1 at the Advanced Light Source. The individual spin and orbital moments were calculated using the sum rules [19], where the number of 3*d* holes was determined from the theoretical calculations. Spin-polarization was measured experimentally by Andreev reflection, based on the methods described in [20]. Conversion electron Mössbauer spectrometry (CEMS) was performed on crystalline ($x = 0.77$–0.55) and amorphous ($x = 0.67$) Fe_xSi_{1-x} thin films at 300 K. Further measurement details and results are discussed in the supplementary material and references [21].

Theoretical calculations were performed on amorphous and crystalline structures. *Ab initio* molecular dynamics (MD) simulations and density functional theory (DFT) were used to simulate the amorphous structure in a cubic unit cell of volume *V* containing 128 atoms ($128*x$ Fe atoms and $128*(1-x)$ Si atoms) using the plane-wave-based Vienna *ab initio* simulation package (VASP) [22], with the projector augmented wave (PAW) method for the description of core-valence interaction [23]. The exchange-correlation functions were treated at the level of generalized-gradient approximation [24]. The structure underwent a melting (2000 K), a quenching (2000–200 K at 3×10^{14} K s^{-1}), and annealing (200 K, 5 ps) step in a canonical ensemble for the randomization of atomic structural positions. The atomic spacing, positions and *V* were further optimized before and after the quenching and annealing processes, until forces on each atom were less than 0.01 eV Å^{-1}. An energy cutoff of 350 eV was used for the expansion of plane-wave basis functions. While only the Γ-point was used to sample the Brillouin-zone during the melting, quenching and annealing processes, $3 \times 3 \times 3$ Monkhorst-Pack *k*-points were used for the geometry relaxation and electronic structure determination after the MD simulations. For the crystalline Fe_xSi_{1-x} alloys, supercell models with 16 atoms were used. Both $D0_3$ and B2-like structures were investigated for $x = 0.75$. For $x = 0.625$ and 0.6875, some body center Fe atoms of the stoichiometric $D0_3$ unit cell were replaced by Si, forming off-stoichiometry $D0_3$-like structures; all the body center atoms were randomized to form B2-like structures. The lattice constants of these simulated structures were within 1% of the experimental values. The A2 structure, although not experimentally realized, was also calculated for $x = 0.65$. Magnetization, atomic density, electronic band structure, and pair distribution functions were calculated for each structure.

---

[9] It was not possible to grow amorphous films at higher *x* or epitaxial films at lower *x*.

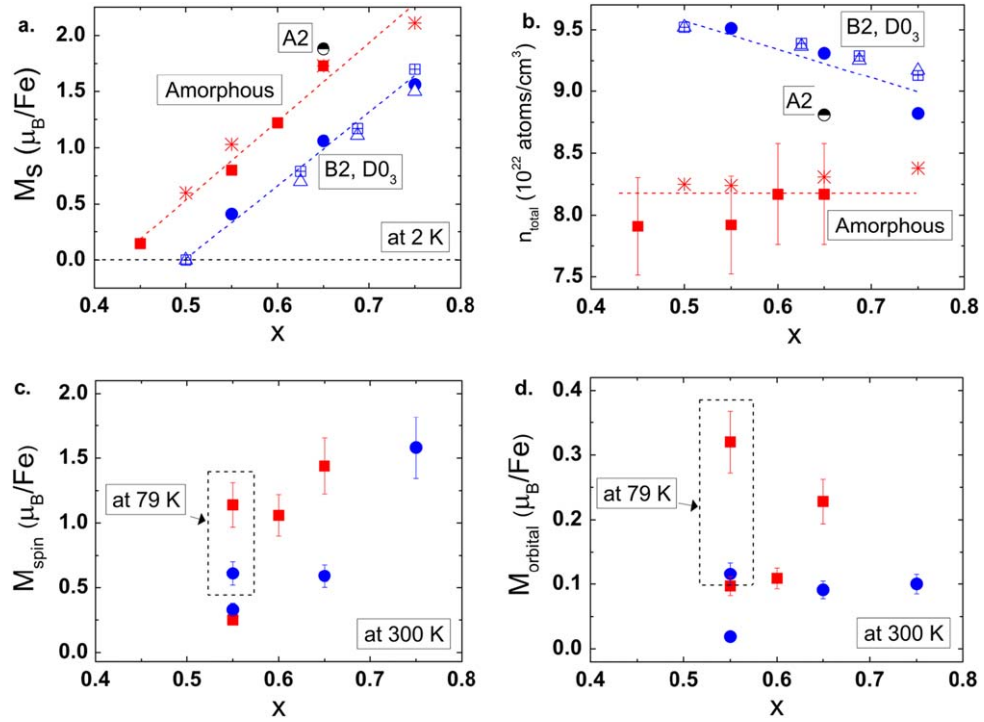**Figure 1.** (a) Magnetization at 2 K (b) total number density, (c) spin and (d) orbital moments at 300 K versus Fe concentration for $Fe_x Si_{1-x}$ amorphous and crystalline materials. Solid symbols are experimental data: amorphous films (red squares) and epitaxial films (blue circles). In (c) and (d) the $x = 0.55$ data enclosed by a box is at 79 K. Open symbols are theory: amorphous (red stars), A2 (half filled black circle), B2 (blue triangle), D0$_3$ (blue square with cross). The red and blue dashed lines are a guide to the eye. Where error bars are not shown, the error is smaller than the size of the data points.

Figure 1 shows theoretical and experimental spontaneous magnetization, M_s, (M at high H extrapolated to $H = 0$) at 2 K (a) and n_{total} (b) versus x for crystalline and amorphous films. Square hysteresis loops are observed for all $x \geqslant 0.55$, indicating the samples are ferromagnetic. The shape of the $M(H)$ curve for the amorphous $x = 0.45$ sample is not square; however, magnetic remanence is found and M is larger than a Brillouin function, indicating weak ferromagnetism (see supplementary material). Strikingly, for all x in theory and experiment, M_s of the amorphous samples is very large in comparison to crystalline (B2, D0$_3$) samples with the same compositions. The value is dependent on chemical order; the chemically disordered theoretical A2 structure has a significantly larger moment than B2 or D0$_3$, which are the same for a given x. In the B2 and D0$_3$ structures, the nearest neighbor environments are the same and only the second nearest neighbors, which have a smaller effect on M, differ. In figure 1(b), as x increases, the theoretical and experimental n_{total} of the crystalline films decreases. By contrast, n_{total} of the amorphous films is constant with composition and significantly (13–17%) lower than the crystalline films at all x.

To understand the enhanced magnetism at the atomic level, XMCD (at 79 K, 300 K) was used to experimentally determine the Fe spin (M_{spin}) and orbital ($M_{orbital}$) moments, which were calculated based on the methods described in references [19, 25]. Figures 1(c) and (d) show M_{spin} and $M_{orbital}$, respectively, for both amorphous and epitaxial films. M_{spin} and $M_{orbital}$

calculated for epitaxial $x = 0.75$ and 1.0 films are in good agreement with previous reports [19, 26]. For all x, M_{spin} tracks the total M and is significantly larger in the amorphous than crystalline films. Even for $x = 0.55$, whose spin moments at 300 K are near zero since T_c is near 300 K, measurements at 79 K show that the amorphous film exhibits a much larger M_{spin} than the epitaxial film. The amorphous films' $M_{orbital}$ also increase with increasing x and are larger than the crystalline samples with the same composition, likely due to the lower local symmetry of the amorphous phase.

To explain the enhancement in M_{spin} we turn to an investigation of the local atomic structure of the amorphous films, which was analyzed in the DFT calculations using pair correlation functions and experimentally by XAFS at the Fe K-edge (see supplementary material). The number of Fe-Fe (Fe-Si) pairs in the i shell of nearest neighbors is defined as N_{Fe-Fe}^{i} (N_{Fe-Si}^{i}), and the total coordination number in the i shell is CN^i. In both theory and experiment, no Fe-Fe pairs were observed in the first shell for $x = 0.50$ or 0.55. Fe atoms are completely surrounded by Si but with fewer Si atoms than in the crystalline structures (except for the theoretical A2 phase). As shown in figure 2, for higher x, N_{Fe-Fe}^{1} increases with x while N_{Fe-Si}^{1} decreases causing CN^1 to only slightly increase. The total coordination numbers $CN^1 (\sim 6)$ and $CN^2 (\sim 12)$ are significantly smaller for all x than the corresponding values, 8 and 14, respectively, in the bcc structure and significantly less than the fcc value ($CN^1 = 12$) suggested previously in a-Fe$_x$Si$_{1-x}$ (see supplementary material) [15]. Not just the reduced coordination but also the nearest neighbor species play a crucial role in the magnitude of the moment; notably, it is not the number of Fe nearest neighbors that determines the magnetic moment of an Fe atom but the number of Si neighbors.

This point is elucidated in figure 2, which compares the experimental and theoretical average number of first shell Fe and Si neighbors for selected amorphous and crystalline (A2, B2, D0$_3$) compositions. N_{Fe-Fe}^{1} (figure 2(a)) in the crystalline materials is greater than in the amorphous materials for all x, hence striking and not immediately obvious why the moment in the crystalline systems is LESS than in the amorphous. However, N_{Fe-Si}^{1} (figure 2(b)) is also greater in the crystalline materials, for all x; therefore, the enhanced magnetism in the amorphous compositions can only be explained by the fact that N_{Fe-Si}^{1} is less. As an example, consider $x = 0.5$, where both the amorphous and crystalline structures have no Fe nearest neighbors. The B2 phase has no moment while the amorphous films have a significant moment. In the B2 phase, all 8 Fe nearest neighbors are Si, whereas in the amorphous structure, there are only 5 Si neighbors. Only in the hypothetical A2 structure would the moment be expected to be larger than the amorphous structure due to its reduced N_{Fe-Si}^{i} relative to the B2, D0$_3$, and amorphous structures (as seen in figure 1 for the calculated value of moment for A2 structure for $x = 0.65$).

Utilization of amorphous Fe$_x$Si$_{1-x}$ thin films as spin injectors also requires consideration of the electronic structure and spin polarization. Figure 3(a) displays the calculated electronic density of states, $D(E)$, for both up (↑) and down (↓) spins for various x in the amorphous structures, and figure 3(b) shows $D(E)$ for the D0$_3$, B2, A2 and amorphous structures with compositions near $x = 0.65$. Spin-splitting is observed in the amorphous bandstructures, although the vanishing of $D\downarrow(E)$ near E_F seen in both B2 and D0$_3$ is lost. Sharp features in the B2 and D0$_3$ structures (figure 3(b)) are significantly broadened in the chemically disordered A2 phase, and further broadened in the amorphous structures.
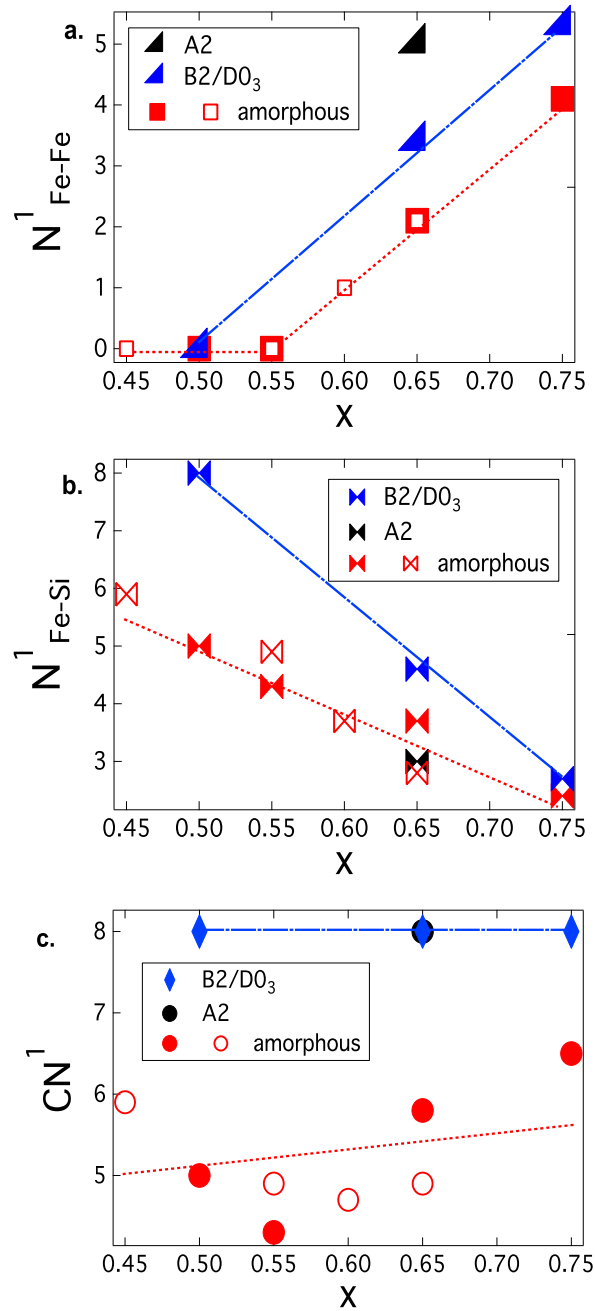
Figure 2. Average (a) $N^1_{\text{Fe-Fe}}$, (b) $N^1_{\text{Fe-Si}}$ and (c) CN^1 for amorphous and crystalline (A2, B2/D0$_3$) materials with various *x*. Open symbols are experimental data, and closed symbols are theory. The lines are a guide to the eye. In (c) the A2 and B2/D0$_3$ data points for *x* = 0.65 lie on top of each other (i.e. all bcc-like structures have 8 nearest neighbors).
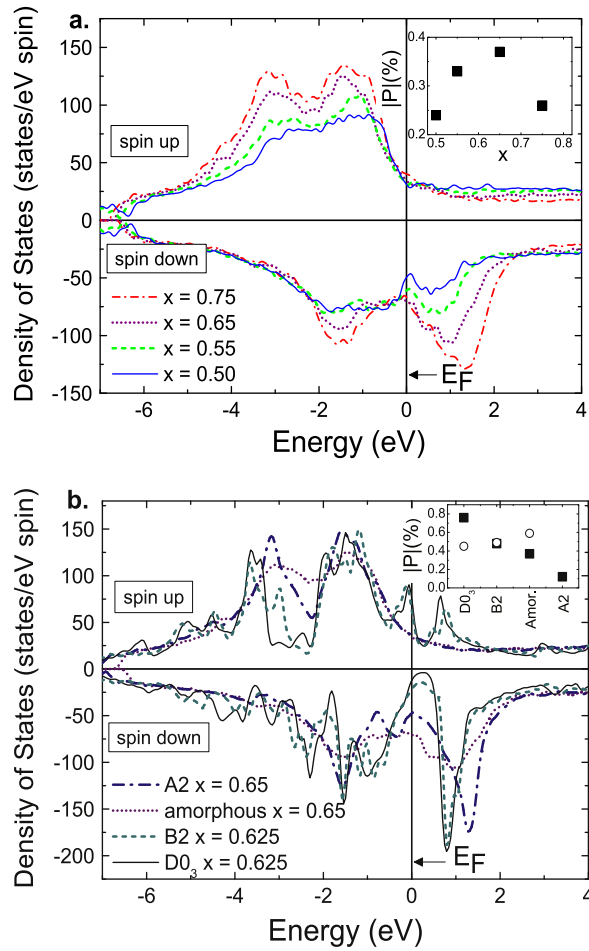
Figure 3. Calculated density of states for (a) amorphous structures with various compositions ($x = 0.5$–0.75) and (b) crystalline and amorphous structures near $x = 0.65$. Insets: absolute value of spin-polarization $|P|$ at E_F from (a) theoretical calculations (black squares) for amorphous structures with various x and (b) theoretical calculations (black squares) and Andreev reflection (open circles) for crystalline and amorphous structures with $x \sim 0.65$. Note that experimental and theoretical values of $|P|$ for the B2 structure are the same. The $D0_3$ open circle in the inset of (b) is an experimental Andreev reflection data point for $D0_3$ $x = 0.75$ from [27].

The spin polarization at E_F, $|P|$, is defined as $\left| \left[D\uparrow(E_F) - D\downarrow(E_F) \right] / \left[D\uparrow(E_F) + D\downarrow(E_F) \right] \right|$ and was determined both theoretically from $D(E)$ and experimentally by Andreev reflection (see supplementary material). For the theoretical amorphous structures, $D\uparrow(E_F)$ is relatively insensitive to composition, $D\downarrow(E_F)$ changes only slightly; P is negative and does not significantly change with composition (inset figure 2(a)). As shown in the inset of figure 3(b), the calculated spin polarization in the amorphous material ($x = 0.65$) is larger than the A2 structure; it is nearly as large (although of the opposite sign) as the B2 structure. The experimental spin polarization is also shown in the inset of figure 3(b) for an amorphous film ($x = 0.65$) and epitaxial film ($x = 0.65$). $|P|$ measured is

larger in the amorphous film than the epitaxial film. In fact, the spin polarization is larger than a previously reported value for a $D0_3$ $x = 0.75$ epitaxial film [27].

In summary, structural disorder was used to tune the magnetic and electronic properties of Fe_xSi_{1-x} thin films. Enhanced magnetic moment and spin polarization were observed for all amorphous films compared to crystalline films of the same composition. Experimental and DFT results showed decreased number densities and coordination numbers in the amorphous structures in comparison to the crystalline phases. The reduced coordination and density of the amorphous Fe-Si structure preserves a ferromagnetic Fe-Fe exchange coupling with no frustration, unlike other amorphous Fe-based materials. The local atomic structure in the amorphous materials has fewer Fe-Si pairs than in any chemically ordered crystalline material but with interatomic distances that are comparable to bcc structures, resulting in the observed moment enhancement and ferromagnetic exchange interactions. This local structure in the amorphous system also preserves a surprisingly robust spin-polarization. Remarkably, disorder significantly enhances the magnetic properties in this amorphous structure, making this material potentially relevant as a spin injector.

References

[1] Walterfang M, Keune W, Trounov K, Peters R, Ruecker U and Westerholt K 2006 *Phys. Rev.* B **73** 214423
[2] Berling D, Gewinner G, Hanf M C, Hricovini K, Hong S, Loegel B, Mehdaoui A, Pirri C, Tuilier M H and Wetzel P 1999 *J. Magn. Magn. Mater.* **191** 331
[3] Hines W A, Menotti A H, Budnick J I, Burch T J, Litrenta T, Niculescu V and Raj K 1976 *Phys. Rev.* B **13** 4060
[4] Kudrnovsky J, Christensen N E and Andersen O K 1991 *Phys. Rev.* B **43** 5924
[5] Gray A X *et al* 2011 *Phys. Rev.* B **83** 195112
[6] Coey J M D 1978 *J. Appl. Phys.* **49** 1646
[7] Moorjani K and Coey J M D 1984 *Magnetic Glasses* (New York: Elsevier)
[8] Raeburn S J and Aldridge R V 1978 *J. Phys F.: Metal Phys.* **8** 1917
[9] Felsch W 1969 *Z. Physik* **219** 280
[10] Ohta M, Fujita A and Kukamichi K 2000 *J. Alloys Compd.* **308** 38
[11] Malozemoff A P, Williams A R, Terakura K, Moruzzi V L and Fukamichi K 1983 *J. Magn. Magn. Mater.* **35** 192

[12] Goto T, Kuroda K, Komatsu H and Fukamichi K 1992 *J. Magn. Magn. Mater.* **104-107** 135

[13] Coey J M D, Givord D, Lienard A and Rebouillat J P 1981 *J. Phys. F.: Metal Phys.* **11** 2707

[14] Heiman N and Kazama N 1979 *Phys. Rev.* B **19** 1623

[15] Marchalt G, Mangin P, Piecucht M, Janott C and Hubsch J 1977 *J. Phys. F: Metal Phys.* **7** L165

[16] Mangin P, Marchal G, Rodmacq B and Janot C 1977 *Philos. Mag.* **36** 643

[17] Mangin P and Marchal G 1978 *J. Appl. Phys.* **49** 1709

[18] Manyala N, Sidis Y, DiTusa J F, Aeppli G, Young D P and Fisk Z 2004 *Nature Mater.* **3** 255

[19] Chen C T, Idzerda Y U, Lin H-J, Smith N V, Meigs G, Chaban E, Ho G H, Pellegrin E and Sette F 1995 *Phys. Rev. Lett.* **75** 152

[20] Chen T Y, Huang S X and Chien C L 2010 *Phys. Rev.* B **81** 214444

[21] Karel J, Juraszek J, Minar J, Bordel C, Stone K, Jenkins C A, Arenholz E, Ebert H, Kortright J B and Hellman F to be published

[22] Kresse G and Furthmüller J 1996 *Phys. Rev.* B **54** 11169

[23] Blöchl P E 1994 *Phys. Rev.* B **50** 17953

[24] Perdew J P, Burke K and Ernzerhof M 1996 *Phys. Rev. Lett.* **77** 3865

[25] Meinert M, Schmalhorst J, Wulfmeier H, Reiss G, Arenholz E, Graf T and Felser C 2011 *Phys. Rev.* B **83** 064412

[26] Krumme B *et al* 2009 *Phys. Rev.* B **80** 144403

[27] Ionescu A *et al* 2005 *Phys. Rev.* B **71** 094401

Supplementary Material

Sample Characterization

For the amorphous films, XRD showed no crystallinity for all $x \leq 0.67$. High resolution transmission electron microscopy (HRTEM) for an $x=0.67$ sample showed partial crystallinity (nanocrystals <2 nm in an amorphous matrix), and for $x=0.55$ showed only occasional small areas of poorly defined lattice fringes. For the crystalline films, X-ray diffraction (XRD) θ-2θ scans showed only the 100 and 200 peaks (referenced to bcc structure) out of plane. ϕ scans on the 220 off-axis peak showed sharp peaks (FWHM ~2-3°) with the expected four-fold symmetry of an epitaxial film, and reflection high energy electron diffraction (RHEED) patterns taken immediately after growth were streaky, confirming epitaxial films. The presence of the 100 peak indicates B2 or D0$_3$ chemical order since this peak would be absent in the A2 structure. The ratio of the 100 to 200 integrated peak intensities was 0.022, 0.043, and 0.099 for $x=0.75$, 0.65, and 0.55, respectively, which represents good chemical order (comparable to theoretical ratios of 0.03, 0.06, and 0.11 for these values of x). Note that the 100/200 peak ratio is identical for the D0$_3$ and B2 structures, even off stoichiometry, due to the nature of their chemical ordering. The coherence length of the chemical order and structural order, as calculated from the width of the 100 and 200 peaks respectively, is ~240 Å for all x studied. The chemical ordering was determined by conversion electron Mössbauer spectrometry (CEMS) to be B2 (CsCl) for $x \leq 0.67$ and D0$_3$ for $x>0.67$.[1] Films with the A2 structure were not successfully fabricated (but have been theoretically modeled).

Magnetic Properties

Figure S1 shows $M(H)$ curves at 2 K for all amorphous compositions investigated; square hysteresis loops were observed for $x \geq 0.55$. Samples with compositions $x \geq 0.60$ are ferromagnetic at room temperature, and samples with $x<0.60$ are above or near their transition at room temperature. We find the onset of ferromagnetism (based on extrapolation of M_s vs x to zero) occurs in the amorphous system at $x \sim 0.42$, consistent with previous work.[2] The amorphous $x=0.45$ sample (inset) is near this critical composition, and the shape of the curve is different than the samples with higher x. Figure S2 shows that M at all H of the $x=0.45$ sample is significantly larger than a Brillouin function with S=3/2 (and is even larger than S=1/2), indicating weak ferromagnetism.
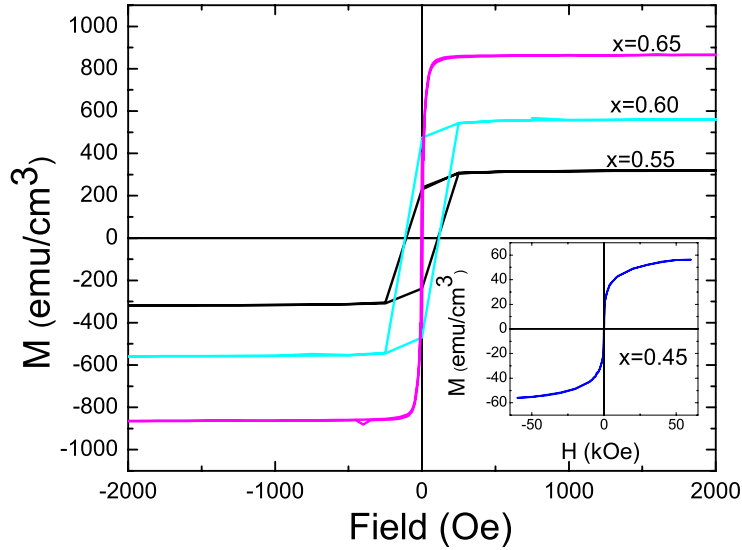
Figure S1. $M(H)$ at 2 K for amorphous Fe_xSi_{1-x} with x = 0.55, 0.6, 0.65. The inset shows x=0.45 on an expanded scale.
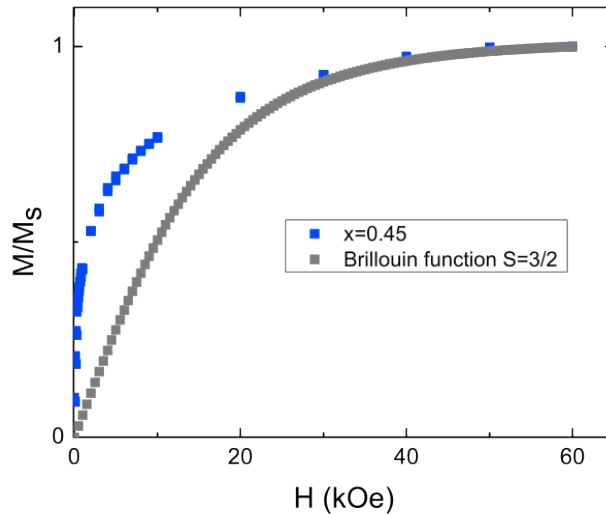

Figure S2. Comparison of $M(H)$ at 2K of amorphous x=0.45 sample to Brillouin function with S=3/2. Note the experimental data are also larger than the S=1/2 Brillouin function, which is not shown.

Local Atomic Structure

Pair Correlation Functions
Pair correlation functions (PCFs) are the number of *e.g. A-B* pairs in the spherical shell ranging from r to $(r + dr)$ around one A-type atom. There are three partial PCFs and one total PCF for the Fe_xSi_{1-x} binary alloys: $g_{Fe\text{-}Fe}(r)$, $g_{Fe\text{-}Si}(r)$, $g_{Si\text{-}Si}(r)$, and $g_{tot}(r)$. The total

coordination number in the first (CN^1) or second (CN^2) shell is determined by integrating $g_{tot}(r)$ to the radius at the minimum of the first (for CN^1) or first + second (for CN^2) Gaussian. Similarly, the number of Fe-Fe (Fe-Si) pairs in the i shell of nearest neighbors N^i_{Fe-Fe},(N^i_{Fe-Si}) can be determined from the integral of $g_{Fe-Fe}(r)$ ($g_{Fe-Si}(r)$). The total pair correlation function, $g_{tot}(r)$, is shown in black in figure S3a and S3b for amorphous alloys $x=0.55$ and $x=0.65$. Broad peaks are observed instead of the sharp lines of the crystalline phase, consistent with the simulated amorphous structure. The first peak of $g_{tot}(r)$ can be fit to two Gaussians (green and blue lines), corresponding to the first and second shells of atoms. Relative to the magenta peaks from D0$_3$ Fe$_3$Si, the positions are shifted to slightly smaller r. The nearest neighbor distance of Fe-Si, r^1_{Fe-Si}, is slightly smaller than that of Fe-Fe, r^1_{Fe-Fe}.

The partial density of states (PDOS) for two Fe atoms in an amorphous structure with different numbers of Fe and Si nearest neighbors was also examined and shown in Figure S4. Both Fe atoms have 7 nearest neighbors, 2 (6) of which are Si for Fe$_A$ (Fe$_B$). The PDOS and the magnetic moment (from integrating up minus down PDOS) is significantly different, reflecting that not just the reduced coordination but also the nearest neighbor species play a crucial role in the magnitude of the moment. While in this case both the number of Fe and Si nearest neighbors change, it is not the number of Fe nearest neighbors that determines the magnetic moment but rather the number of Si neighbors (as discussed in the main text).

Figure S5 displays both DFT-calculated and XAFS- experimental N^1_{Fe-Fe}, N^1_{Fe-Si} and CN^1 (a) and DFT-calculated N^2_{Fe-Fe}, N^2_{Fe-Si} and CN^2 (b) versus x (see discussion in main text). The experimental results are discussed next.
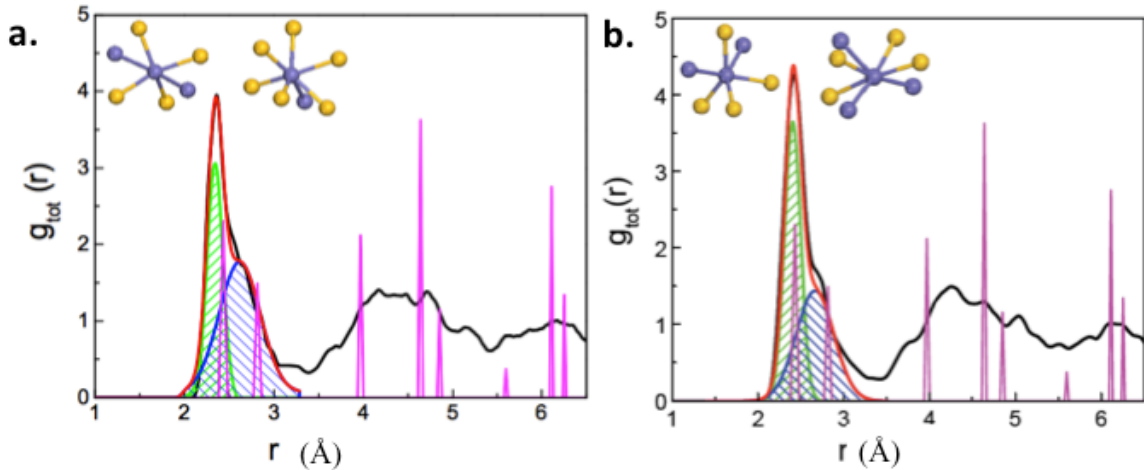

Figure S3. The calculated total pair correlation function, $g_{tot}(r)$, (black) of Fe$_x$Si$_{1-x}$ amorphous alloys, (a) $x=0.55$ and (b) $x=0.65$. The green and blue shades display the fitted Gaussians of the first peak, and the red is the sum of the two fits. The $g_{tot}(r)$ of D0$_3$ Fe$_3$Si is represented by the magenta lines. The insets display two typical structures of Fe (blue) and Si (yellow) atoms around an Fe atom within 2.3~2.6 Å.
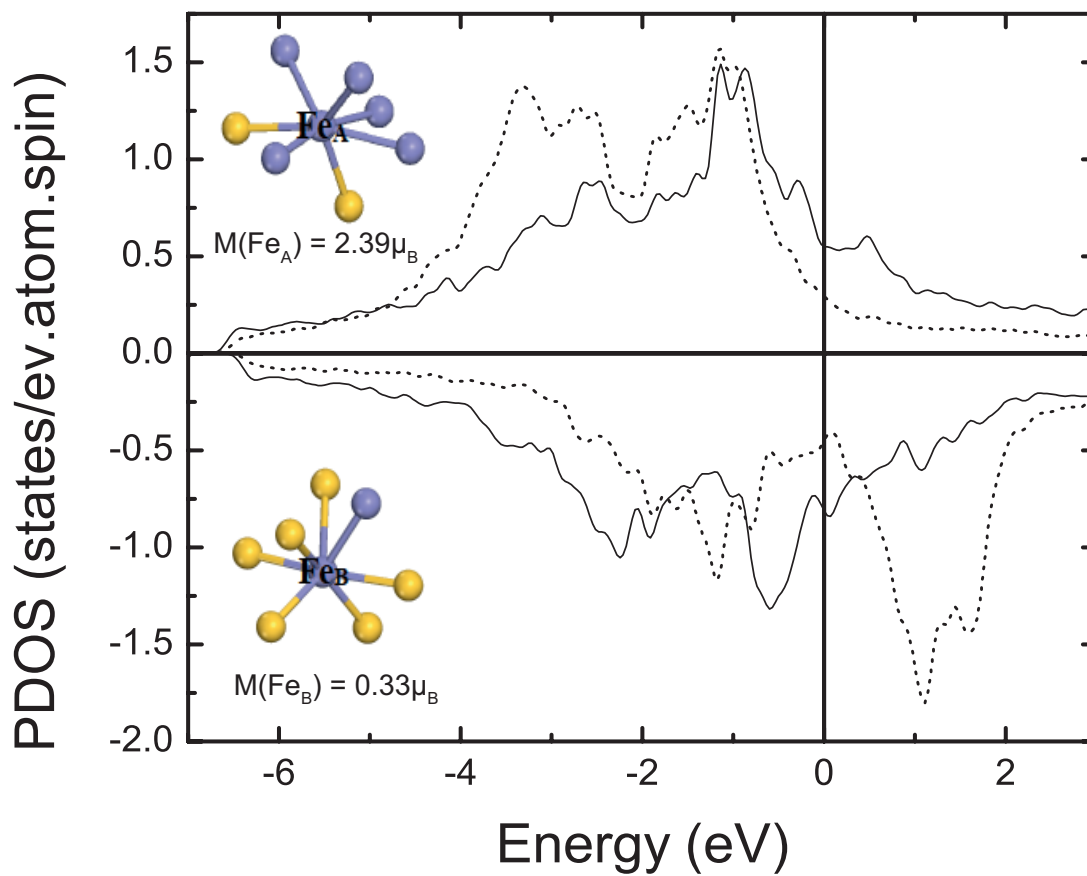
Figure S4. Partial density of states (PDOS) for two Fe atoms (Fe$_A$ and Fe$_B$) in the amorphous structure with different numbers of Fe and Si nearest neighbors, as shown. The Fe atoms are blue, and the Si atoms are yellow in the inset. The dashed (solid) PDOS corresponds to Fe$_A$ (Fe$_B$).
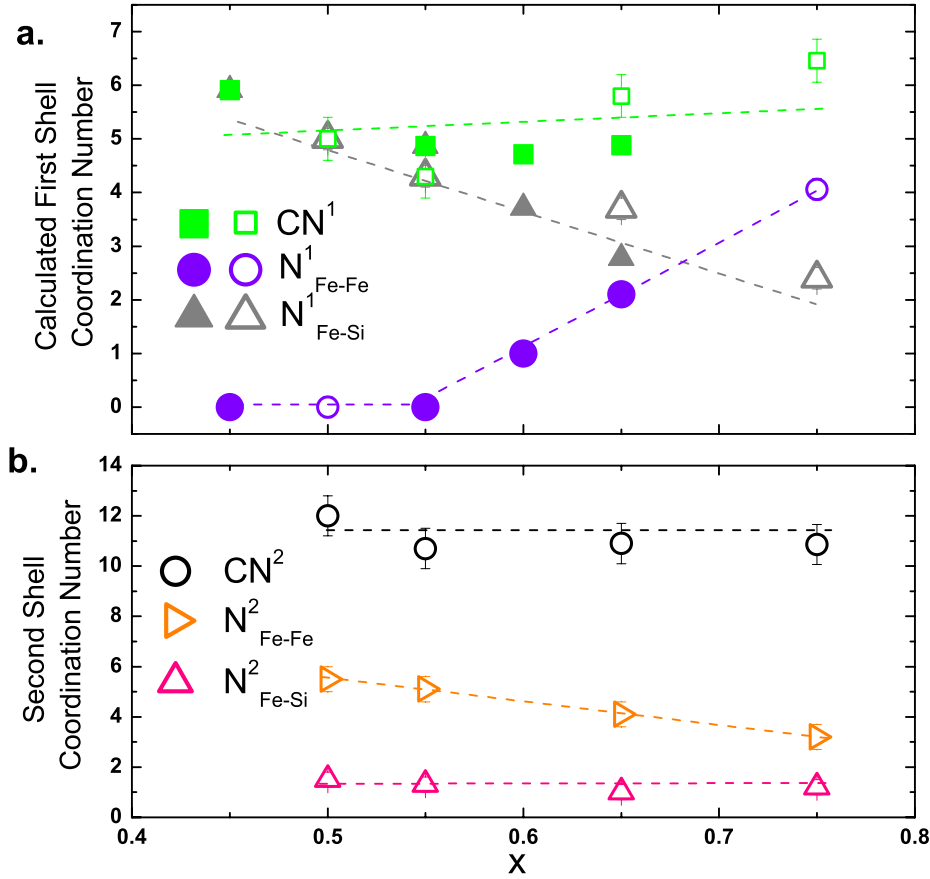
Figure S5. (a) Experimental (XAFS) and DFT-calculated first shell and (b) DFT-calculated second shell local environments versus x for amorphous Fe_xSi_{1-x}. Open symbols are theoretical calculations, and closed symbols are experimental data. All lines are guides to the eye. Error bars if not shown are smaller than the size of the data points. Note for $x=0.65$ N^1_{Fe-Fe}, the theoretical and experimental data points lie on top of eachother. Second shell experimental data for N^2_{Fe-Fe}, N^2_{Fe-Si} and CN^2 is not included because the error bars are too large to be meaningful.

X-ray Absorption Fine Structure (XAFS)

X-ray absorption fine structure (XAFS) was measured at beamline 20-BM-XOR at the Advanced Photon Source (APS), Argonne National Laboratory (ANL), Argonne, IL; room temperature measurements were performed at the Fe K-edge in X-ray fluorescence mode with a Vortex Si drift detector. XAFS data were fit in R-space using FEFFIT with theoretical scattering amplitudes and phase shifts calculated by FEFF.[3,4] Figure S6 shows the fit to the experimental X-ray absorption fine structure data, $\chi(R)$ and $\chi(k)$, for $x=0.45$. The R-range used in the fit was 1-3 Å. All the fits were of similar good quality. The number of first and second nearest neighbors around an Fe atom (N^1_{Fe-Fe}, N^1_{Fe-Si} and N^2_{Fe-Fe}), the first and second nearest neighbor mean square bond length disorder, ($[\sigma^1_{Fe-Fe}]^2$, $[\sigma^1_{Fe-Si}]^2$ and $([\sigma^2_{Fe-Fe}]^2)$ and the first and second nearest neighbor distances (r^1_{Fe-Fe}, r^1_{Fe-Si} and r^2_{Fe-Fe}) are determined from the fits and are given in Table S1. Additionally, figure S5 shows N^1_{Fe-Fe}, N^1_{Fe-Si} and CN^1 (a) and N^2_{Fe-Fe}, N^2_{Fe-Si} and CN^2 (b) versus x. For all compositions, the fitting routine yields only Si in the first shell if all parameters were

allowed to vary. This result of only Si first nearest neighbors is consistent with DFT for x=0.45 and 0.55 (meaning $N^1_{Fe\text{-}Fe}$ = 0), but DFT showed a small number of Fe-Fe first nearest neighbors for x=0.60 and 0.65 (e.g. $N^1_{Fe\text{-}Fe}$ = 2.1 for x=0.65). Note that the mean square bond disorder for Fe-Si nearest neighbors, $[\sigma^1_{Fe\text{-}Si}]^2$, is very low, almost an order of magnitude lower than for Fe-Fe nearest neighbors, indicating that the Si neighbors around each Fe atom are significantly more structurally ordered than the Fe neighbors in the amorphous system. The Fourier transformed XAFS signal shown in figure S7 decreases with increasing Fe concentration, meaning ordered Si is contributing the most to the XAFS signal. A further indication of Si neighbors order is the presence of a second shell of Fe (for $x{\le}0.55$), corresponding to the shoulder at approximately R=2.45 Å in figure S7. We therefore attribute the observed lack of Fe-Fe pairs in the fitting routine for x=0.60 and 0.65 to bond length disorder. Since the modulation in X-ray absorption (XAFS signal) relies on constructive interference of backscattered photoelectrons from nearest neighbor atoms back to the original absorber, bond length disorder causes damping of the XAFS signal due to destructive interference from out of phase photoelectrons. To assess this, $N^1_{Fe\text{-}Fe}$ and $r^1_{Fe\text{-}Fe}$ were fixed in the first shell, and $[\sigma^1_{Fe\text{-}Fe}]^2$ was allowed to vary. As we fixed $N^1_{Fe\text{-}Fe}$ at higher values, $[\sigma^1_{Fe\text{-}Fe}]^2$ increased, indicating a range of possible coordination numbers with comparable fit quality. The variation in bond length ($\sqrt{[\sigma^1_{Fe\text{-}Fe}]^2}$) as $N^1_{Fe\text{-}Fe}$ increased was on the order of 0.25-0.26 Å, meaning the first and second shells were no longer distinct. Hence, the theoretical DFT calculations were used as guidance in selecting $N^1_{Fe\text{-}Fe}$ in the fit for $x{\ge}0.60$.

No Si second nearest neighbors around Fe ($N^2_{Fe\text{-}Si}$) were observed if all parameters were allowed to vary in the fitting routine. However, when the fitting routine was constrained to include Si in the second shell, it either yielded unphysical results (e.g. very large $N^1_{Fe\text{-}Si}$) or did not converge, indicating that second shell Si does not contribute to the Fe XAFS signal.
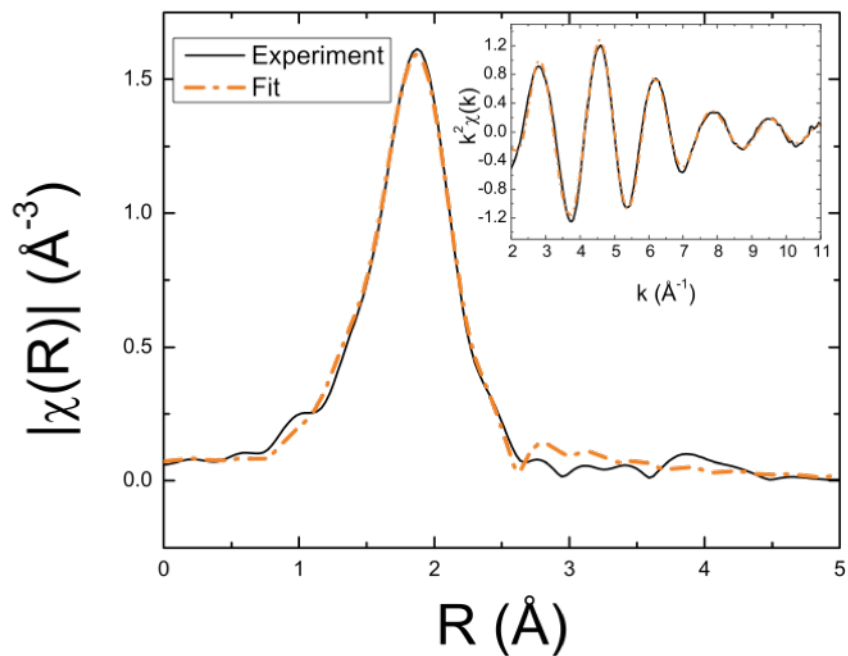
Figure S6. Fourier transformed XAFS |χ(R)| and fit for *x*=0.45. The inset is the XAFS in k-space, weighted by k^2 and the fit.

Atomic % Fe	N^1_{Fe-Fe}	r^1_{Fe-Fe} (Å)	$[\sigma^1_{Fe-Fe}]^2$ (Å²)	N^1_{Fe-Si}	r^1_{Fe-Si} (Å)	$[\sigma^1_{Fe-Si}]^2$ (Å²)	N^2_{Fe-Fe}	r^2_{Fe-Fe} (Å)	$[\sigma^2_{Fe-Fe}]^2$ (Å²)	N^2_{Fe-Si}	r^2_{Fe-Si} (Å)
0.45 XAFS	0	-	-	5.9 ±0.2	2.33 ±0.05	0.009	5.2 ±0.2	2.70 ±0.05	0.02	-	-
0.50 DFT	0	-	-	5.0 ±0.2	2.36 ±0.02	-	5.5 ±0.5	2.74 ±0.02	-	1.5 ±0.3	2.64 ±0.02
0.55 XAFS	0	-	-	4.9 ±0.2	2.34 ±0.05	0.009	5.6 ±0.2	2.67 ±0.05	0.02	-	-
0.55 DFT	0	-	-	4.3 ±0.2	2.34 ±0.02	-	5.1 ±0.5	2.67 ±0.02	-	1.3 ±0.3	2.62 ±0.02
0.60 XAFS	1.0 (fixed)	2.47 (fixed)	0.05	3.7 ±0.2	2.35 ±0.05	0.007	-	-	-	-	-
0.65 XAFS	2.1 (fixed)	2.47 (fixed)	0.05	2.8 ±0.2	2.34 ±0.05	0.006	-	-	-	-	-
0.65 DFT	2.10 ±0.2	2.47 ±0.02	-	3.7 ±0.2	2.38 ±0.02	-	4.1 ±0.5	2.79 ±0.02	-	1.0 ±0.3	2.72 ±0.02
0.75 DFT	4.06 ±0.2	2.50 ±0.02	-	2.4 ±0.2	2.42 ±0.02	-	3.2 ±0.5	2.83 ±0.02	-	1.2 ±0.3	3.03 ±0.02

Table S1. Coordination number, bond length and mean square disorder in bond length from DFT calculations or determined from fits to experimental XAFS data for first shell (grey) and second shell (white).
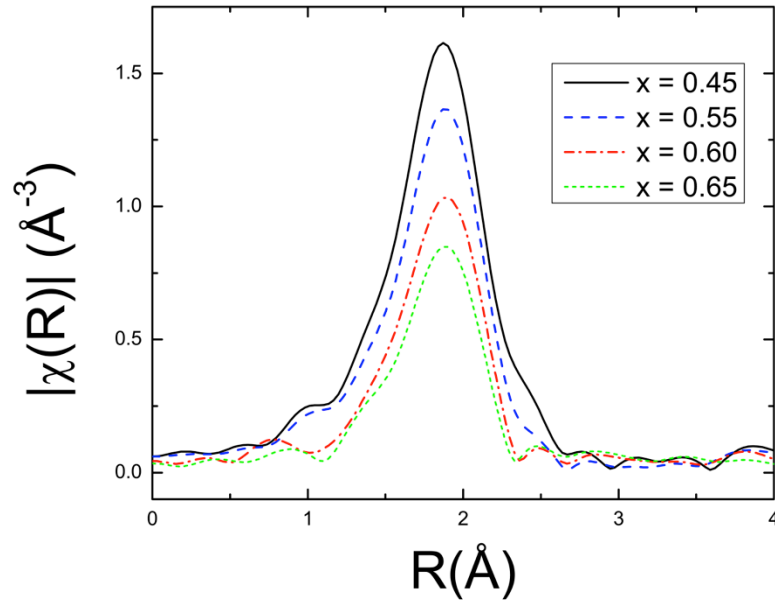
Figure S7. Fe K-edge Fourier transformed XAFS, $|\chi(R)|$, for amorphous Fe_xSi_{1-x} samples of various x.

Point Contact Andreev Reflection

Andreev reflection spectroscopy was performed to compare the spin polarization in amorphous and epitaxial x=0.65 films using either a Nb or Pb tip; no differences were observed between the tip materials. The sample and tip were enclosed in a vacuum jacket and cooled to low temperatures (<3 K), where a point contact was established. Differential conductance (*dI/dV*) and resistance (*V/I*) were measured from over 40 points on the sample using a lock-in method.

Representative Andreev reflection conductance curves are shown in figure S8 for both amorphous and crystalline x=0.65 samples in contact with a Pb tip. The open symbols are experimental data, and the lines are the best fit using the Chen-Tesanovic-Chien (CTC) model, which describes the data well.[5] An additional resistance (r_E), independent of the point contact resistance, which is due in part to the sample resistance, is taken into account in the fitting, based on the methods described in [6]. The values for the temperature and superconducting gap (Δ) are based on the experimental parameters; r_E, the interfacial scattering factor (*Z*) and *P* are determined by the fit. With similar *Z*, the conductance curve for the amorphous sample is much lower in magnitude than that of the crystalline, indicating a much higher spin polarization, as shown in figure 3. The spin polarization values, obtained from the fits to the conductance curves, are plotted as a function of *Z* in figure S9. The spin polarization decreases for increasing *Z* factor. For an ideal interface, *P* is independent of *Z*, however in reality the interfacial barrier always affects *P*.[5] Hence, the intrinsic spin polarization is obtained by extrapolating the *Z* factor

to zero. For the amorphous $x=0.65$ sample, P is 68.5±3.1%, and for the crystalline $x=0.65$ sample, the extrapolation gives 49.2±0.7%.
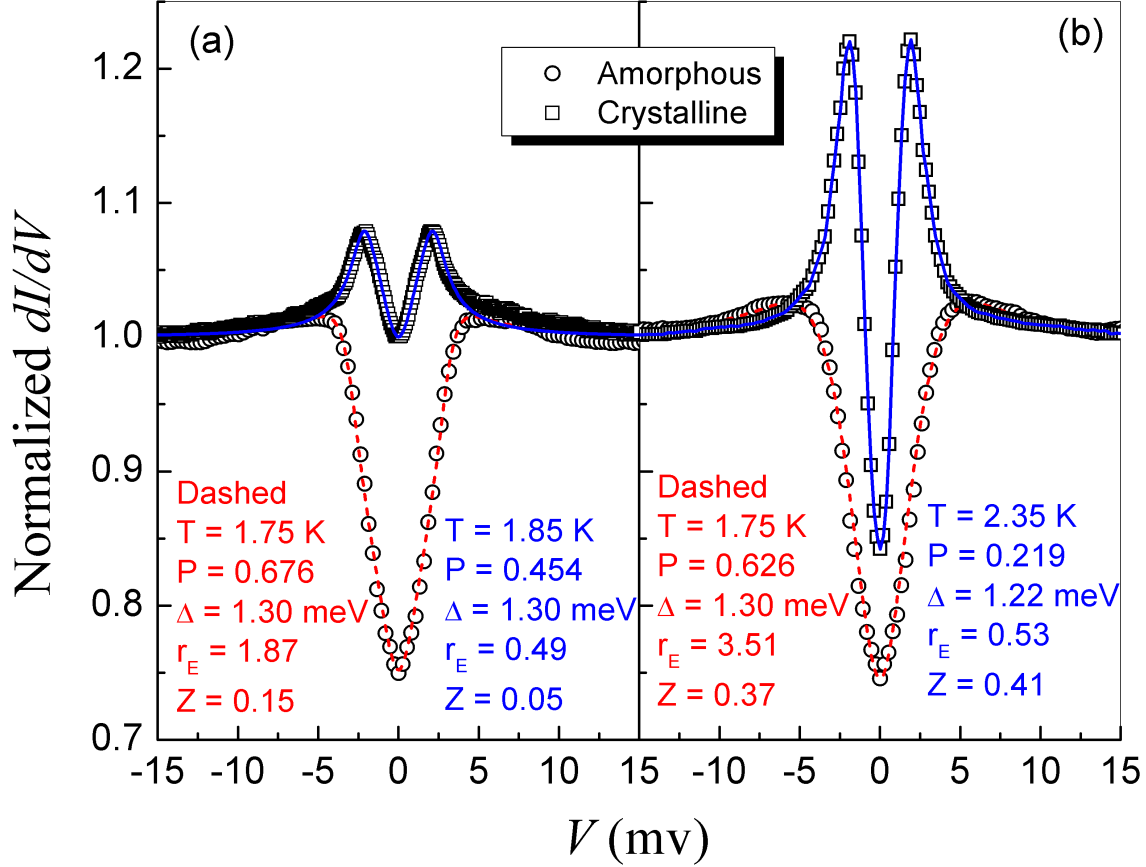

Figure S8. Representative Andreev conductance curves (with Pb tip) obtained from amorphous and crystalline $x=0.65$ samples with **(a)** small interfacial scattering factor (Z) and **(b)** large Z. Z is determined from the fit to the data and varies due to the different point contact measurement positions on the sample. Open squares are experimental data for the crystalline sample; open circles are for the amorphous sample. The solid and dashed lines are the best fit to the data with the parameters listed in the inset.
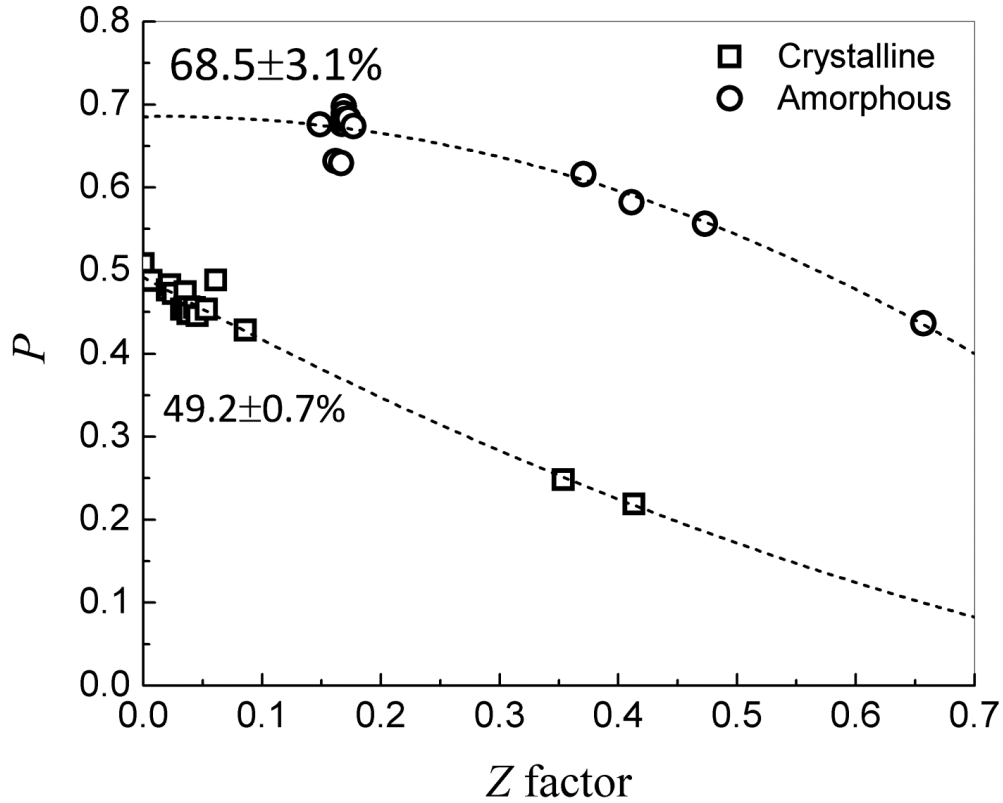
Figure S9. The spin polarization of crystalline (open squares) and amorphous (open circles) *x*=0.65 thin films as a function of Z factor. The dashed lines are a guide to the eye.

References

[1] J. Karel, J. Juraszek, J. Minar, C. Bordel, K. Stone, C.A. Jenkins, E. Arenholz, H. Ebert, J.B. Kortright and F. Hellman, *to be published*
[2] Ph. Mangin, G. Marchal, *J. Appl. Phys.* **49**, 1709 (1978).
[3] M. Newville, B. Ravel, D. Haskel, J.J. Rehr, E.A. Stern and Y. Yacoby, *Physica B* **208/209** 154 (1995).
[4] J.J. Rehr and R. C. Albers, *Rev. Mod. Phys.* **72**, 621 (2000).
[5] T. Y. Chen, Z. Tesanovic, and C. L. Chien, *Phys. Rev. Lett.*, **109**, 146602 (2012).
[6] T. Y. Chen, S. X. Huang, and C. L. Chien, *Phys. Rev. B*, **81**, 214444 (2010).